Using Geophysical Methods to Constrain the Quaternary Activity of the Eastern San Juan Fault

by

Danny Irwin

A Thesis Submitted in Partial Fulfillment of the
Requirements of the

HONOURS PROGRAM

in the School of Earth and Ocean Sciences

Supervisors: Dr. Lucinda Leonard, Dr. Edwin Nissen

University of Victoria

We acknowledge and respect the Lək̓ʷəŋən (Songhees and Xʷsepsəm/Esquimalt) Peoples on whose territory the university stands, and the Lək̓ʷəŋən and W̱SÁNEĆ Peoples whose historical relationships with the land continue to this day.

Contents

1. Abstract

Upper plate faults of southern Vancouver Island have hosted Quaternary earthquakes, posing a significant risk to the densely populated regions of Greater Victoria, Vancouver, and Seattle. The San Juan fault lies adjacent to several faults that have been proven active in the Quaternary, yet its activity remains uncertain due to lack of study. I use a recently available wealth of lidar data to carefully map the eastern part of the fault, looking for intersects between fault lineaments and glacial morphological features. I find a site that is easily accessed by vehicle, where a suspected fault scarp is clearly visible in the lidar data, situated in glacial deposits. Either this scarp formed before the till was deposited, or the scarp formed since the deposition, and is due to either dip-slip and/or strike-slip motion. I perform electrical resistivity tomography, relative gravity, and total magnetic field surveys across the scarp at this location to test these hypotheses, with the resistivity profile showing the most decisive results. Fault structures are observed, and disruptions appear in the uppermost layer, with little visible vertical offset in the till bases, consistent with fault rupture in the Quaternary, with the motion being mostly strike-slip. These findings, combined with similar findings from previous studies further west on the San Juan fault, make a compelling case for further work on the fault, and this location, with its ease of vehicular access, presents the ideal setting.

2. Introduction

2.1 Tectonic Setting of Vancouver Island

Western Canadian seismic activity is dominated by the Cascadia subduction zone, where the Juan de Fuca (JDF) plate moves northeast at $\sim$ 40 mm/yr toward the North American plate, where the cooler, denser oceanic slab is subducted beneath the continental plate (Fig. 2.1)(Harrichhausen et al. 2021, DeMets et al. 2010). This convergent margin runs approximately south-north along the west coast of North America from northern California to the middle of Vancouver Island. The JDF plate is bounded to the west by the Pacific plate, which moves northwest with respect to North America, causing right-lateral shear (McCaffrey et al. 2007). The JDF-Pacific boundary comprises spreading ridges and transform segments.

The Cascadia megathrust has produced great earthquakes in the past. Evidence of a magnitude 9 earthquake in January 1700 CE exists in the form of ghost forests on the west coast of Washington and Oregon from subsidence and saltwater intrusion, buried soils with subsidence evidence and tsunami deposits, an 'orphan' tsunami in Japan, and oral histories from local Indigenous populations (Satake et al. 1996, Nelson et al. 1995). Examination of offshore turbidite records indicates full-length ($\sim$1000 km) rupture events of the Cascadia megathrust, similar to that of 1700, to have average recurrence intervals of 500-530 years, with smaller, M8-8.5 events at intervals of approximately 300 years (Goldfinger et al. 2012, Nelson et al. 1995).

Over the past several decades, much scientific work has been done on southern Vancouver Island to quantify the strain associated with the subduction of the JDF plate under North America (Mazzotti et al. 2003, McCaffrey et al. 2007). Data collected from Global Navigation Satellite Systems (GNSS) surveys across Vancouver Island, western Washington, and Oregon, have shown deformation patterns dominated by interseismic loading along the megathrust zone (Mazzotti et al. 2003, McCaffrey et al. 2007). Velocity vector orientation shows much of Vancouver Island moving northeast relative to stable North America indicating the presence of a strain field due to megathrust locking (Fig. 2.2b), with subduction occurring somewhat perpendicular to the convergent margin (Rahmawan 2026).

The occurrence of future megathrust earthquakes has long been the primary focus of regional seismic hazard assessment. However, Holocene activity has been documented along smaller upper plate fault systems throughout the forearc region (Harrichhausen et al. 2021, Morell et al. 2018,

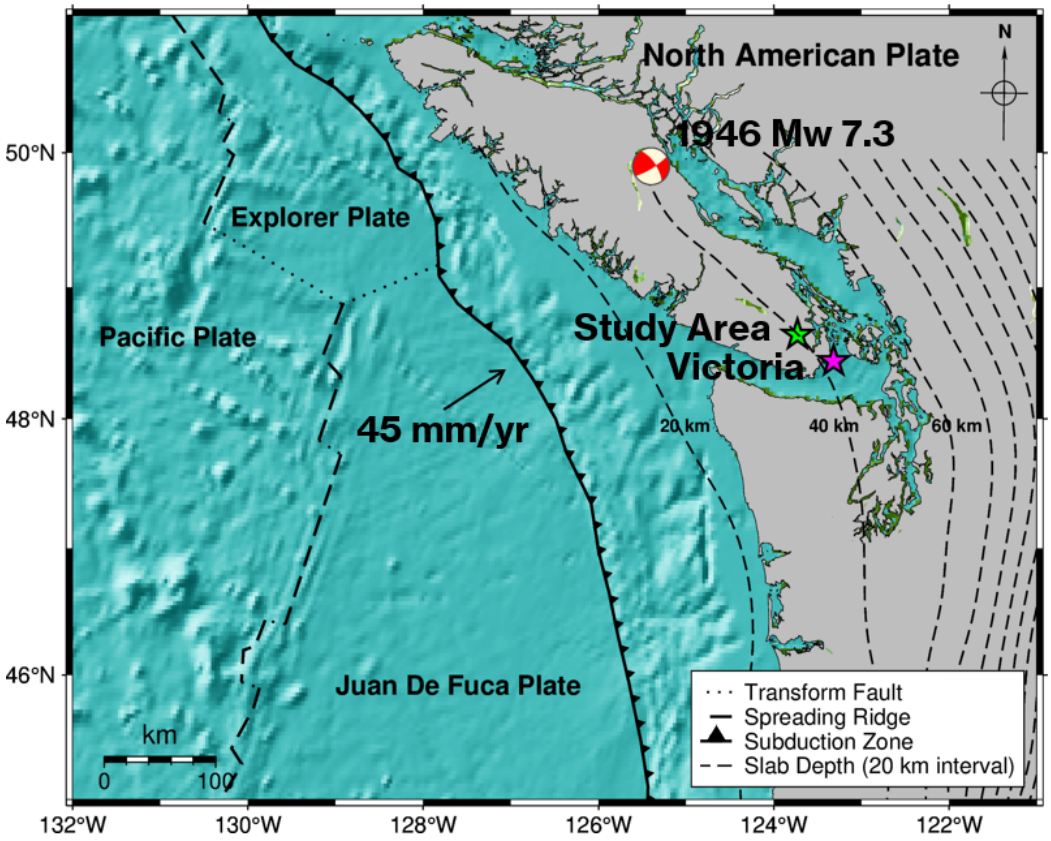

Figure 2.1: Tectonic setting of Cascadia subduction zone, with depth contours of subducted Juan de Fuca slab, from Staisch & Walton (2022)

.

Personius et al. 2014). The largest measured onshore earthquake in recorded Canadian history, M 7.3, occurred on one such fault in the Beaufort Range in 1946 (Fig. 2.1). This earthquake caused two known fatalities and extensive physical damage to local communities (Cassidy et al. 2010, Balfour et al. 2011). Analysis of the Beaufort Range fault has shown that this upper plate fault was a likely candidate to host the earthquake (Lynch et al. 2025). This event, and the discovery of other Quaternary upper plate fault activity in the area motivates the need to assess the Quaternary activity and seismic hazard presented by these faults.

2.2 San Juan Fault

The geology of southern Vancouver Island is largely defined by a succession of terrane accretions ranging from the Mesozoic to Cenozoic eras (Fig. 2.3a). The youngest and southernmost of these terranes, Siletzia, is bounded at the north by the Leech River fault, which was discovered to be

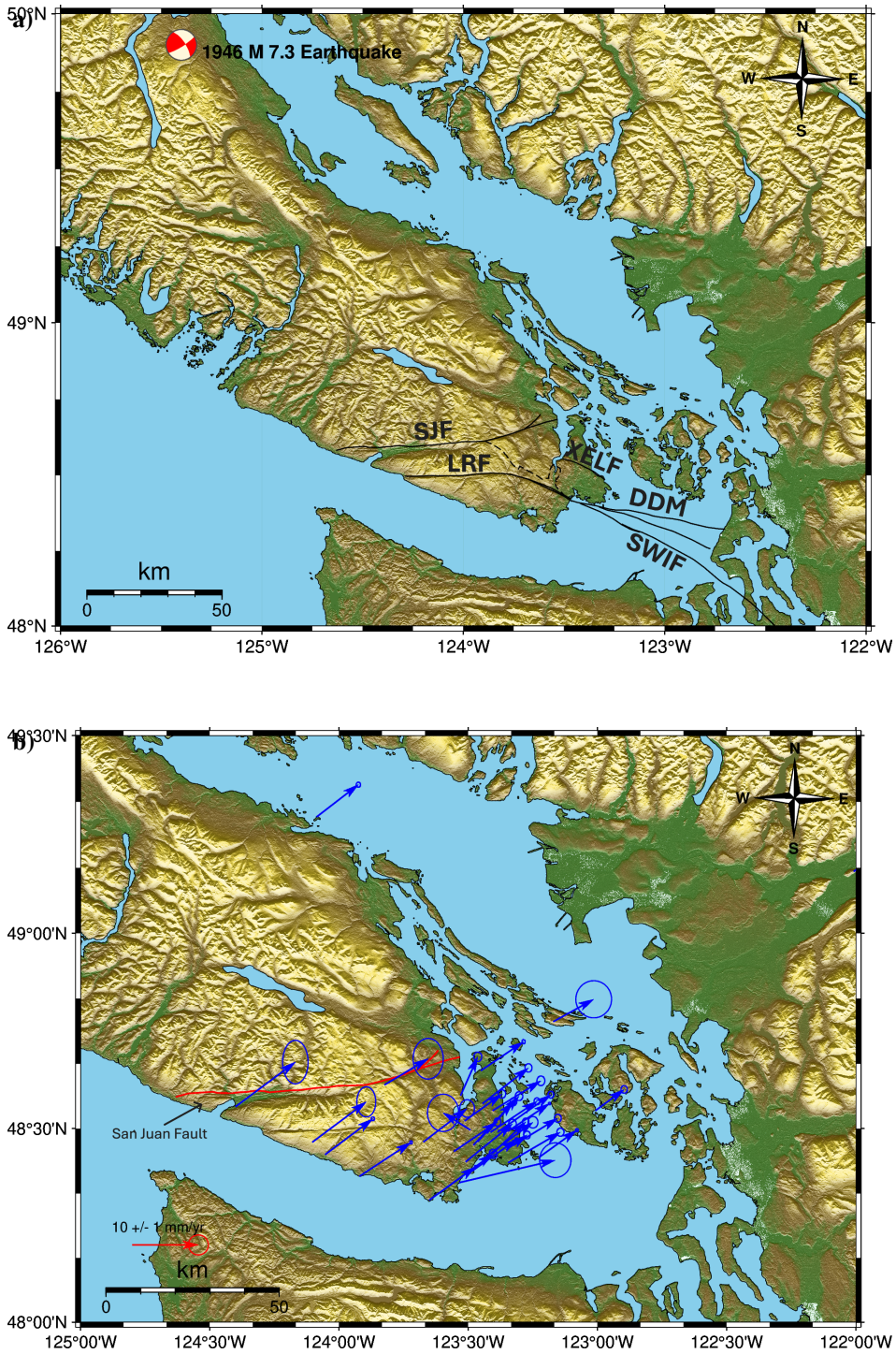

Figure 2.2: **a)** Southern Vancouver Island crustal faults. Mechanism and location of 1946 Beaufort Range earthquake adapted from Lynch et al. (2025). Fault traces adapted from Cui et al. (2017). **b)** GNSS velocity vectors of the Greater Victoria area, relative to stable North America, from Rahmawan et al. (2026). SJF = San Juan fault; XLF = XEOLXELEK-Elk Lake fault; LRF = Leech River fault; DDM = Darrington-Devil's Mountain fault; SWIF = South Whidbey Island fault

Holocene-active, having produced M > 6 earthquakes (Harrichhausen et al. 2021, Morell et al. 2018). Siletzia likely accreted to North America during the Eocene period, and extends south into the Puget Sound and beyond (Harrichhausen et al. 2022). North of the Leech River fault zone lies the Leech River complex, which is part of the Jurassic-Cretaceous Pacific Rim terrane, which is bounded to the north by the western part of the San Juan fault (SJF), and to the east by the Survey Mountain fault (Harrichhausen et al. 2022). The SJF has a largely continuous fault trace, striking WSW-ENE, crossing nearly the breadth of Vancouver Island. The western region of the fault lies on the contact between the Pacific Rim terrane and the older Wrangellia terrane, a broader complex which covers much of Vancouver Island (Harrichhausen et al. 2022, Cui et al. 2017).

Just east of the midpoint of the SJF, the Survey Mountain fault system branches off to the southeast, continuing the contact between the Wrangellia and Pacific Rim terranes (Fig. 2.3a). As the structure continues east, the SJF forms a contact between geologic units within Wrangellia - to the north of the fault lies the Devonian Sicker Group, the oldest unit of Wrangellia, comprised of volcanic basalts and tuff layers (Harrichhausen et al. 2022, Cui et al. 2017); to the south lies the Crystalline Complex of the larger Mesozoic Intrusive Group, comprised largely of diorite, gabbro, and metamorphic units (Cui et al. 2017). The SJF trace then bifurcates again northwest of Shawnigan Lake, with one branch trending SW, and the other trending WSW. The northern branch (which strikes SW) cuts through the Devonian Sicker Group, and the southern branch forms a contact between the Sicker and Bonanza Groups (Harrichhausen et al. 2022, Cui et al. 2017).

The main models of historic motion of the SJF that have been presented are thrust faulting to accommodate upper Jurassic-Cretaceous accretion of the Pacific Rim to Wrangellia (Brandon 1989); left-lateral-dominant faulting to accommodate the same accretion (Rusmore & Cowan 1985); and left-lateral re-activation of the fault during the Eocene accretion of the Sileztia terrane (England & Calon 1991). Work done by Harrichausen et al. (2022) using inversion of fault plane structures, geological mapping, and marine sediment dating demonstrated that the SJF offsets the Pacfic Rim - Wrangellia terrane boundary and was therefore constrained mostly to Eocene activity. More recently, Salomon et. al (2026) interpret right-lateral motion on the SJF based on stepped offsetting of streams in the San Juan valley. These findings agree with the NNW-SSE maximum compressive stress direction in the region (Balfour et al. 2011).

2.3 Assessing Quaternary Activity of the San Juan Fault

Upper plate faults are considered Quaternary-active when ruptures have been demonstrated to show offset in glacial deposits, as opposed to merely juxtaposing older bedrock units. Proving this requires locating sections of the fault trace where post-glacial sediments (till or colluvium) exist, and exhibit clear evidence of fault offset.

Accurate mapping of crustal fault traces on southern Vancouver Island is challenging. Dense vegetation coverage and limited road access present difficulties for ground mapping. In recent years, greater availability of high resolution lidar data from BC Open Lidar Data Portal in the region surrounding the SJF allows a much higher degree of precision in mapping fault traces using digital terrain models (DTMs) which minimize the masking effect of tree coverage (GeoBC 2020). These DTMs have been used to discover previously unknown fault traces (Harrichhausen et al. 2023, Salomon et al. 2026).

Due to its proximity to the communities of Duncan, Shawnigan Lake, and Greater Victoria, attempting to understand the seismic hazard posed by the SJF is extremely important. The nearby Leech River fault, the XEOLXELE~~K~~-Elk Lake fault, and the Darrington-Devils Mountain fault have been shown to host earthquakes as recently as the Holocene (Harrichhausen et al. 2021, 2023, Morell et al. 2018, Personius et al. 2014). The central part of the SJF has shown preliminary evidence of disruption of glacial deposits using electrical resistivity tomography (ERT) surveying over a suspected fault scarp identified in lidar imagery (Salomon et al. 2026). Since this work was done, additional lidar data along the eastern SJF traces around Shawnigan Lake have become available from BC Open Lidar Data Portal, presenting the opportunity for further work of this nature (GeoBC 2020).

In this study, I examine whether the San Juan fault has been active during the Quaternary, and whether the slip was dominantly strike-slip or dip-slip (Fig. 2.4). I use lidar data to map the eastern extent of the SJF trace with high-resolution shaded relief topography, looking in particular for regions where the trace intersects suspected glacial landforms, or where the fault is covered by glacial deposits. I model subsurface structure across the fault trace where it presents as a topological scarp, using various geophysical methods to see if fault structures are observed, whether the structures are strike-slip, dip-slip, or both, and whether they disrupt the youngest layer (Fig. 2.4).

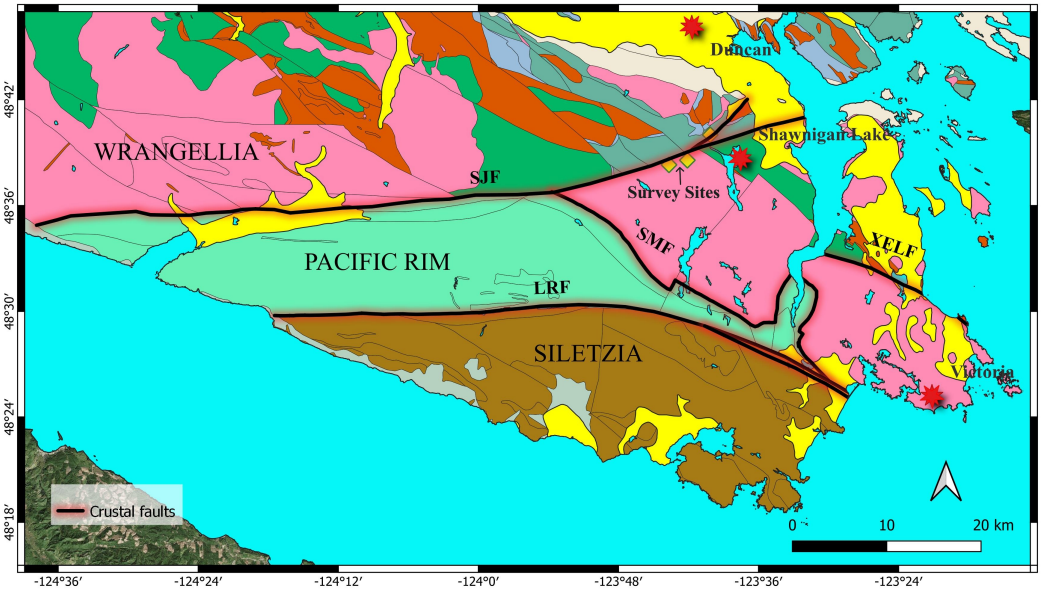

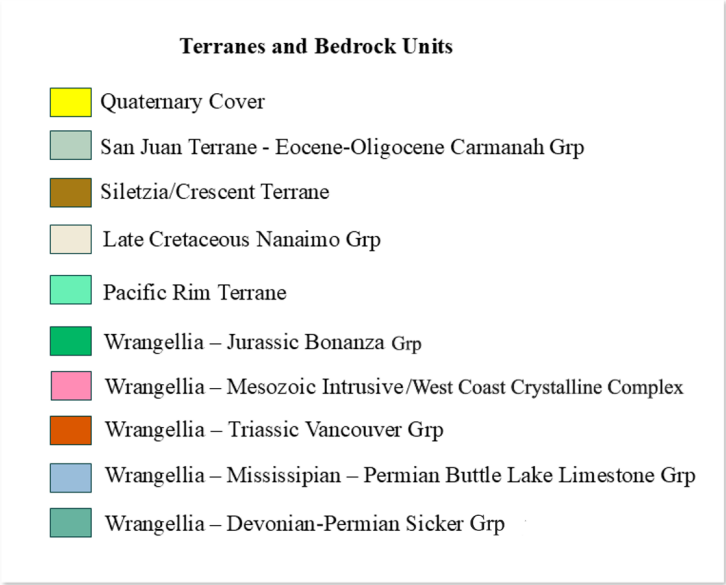

Figure 2.3: Terranes of southern Vancouver Island, with bedrock units and upper plate faults of interest to this study. Diamonds represent survey sites in study area (see Methods below). Bedrock units and ages adapted from Cui et al. (2017) and Harrichhausen et al. (2022). Faults adapted from Cui et al. (2017). Shorelines and coastlines from Messenger et al. (2016) and OpenStreetMap Contributors (2025)

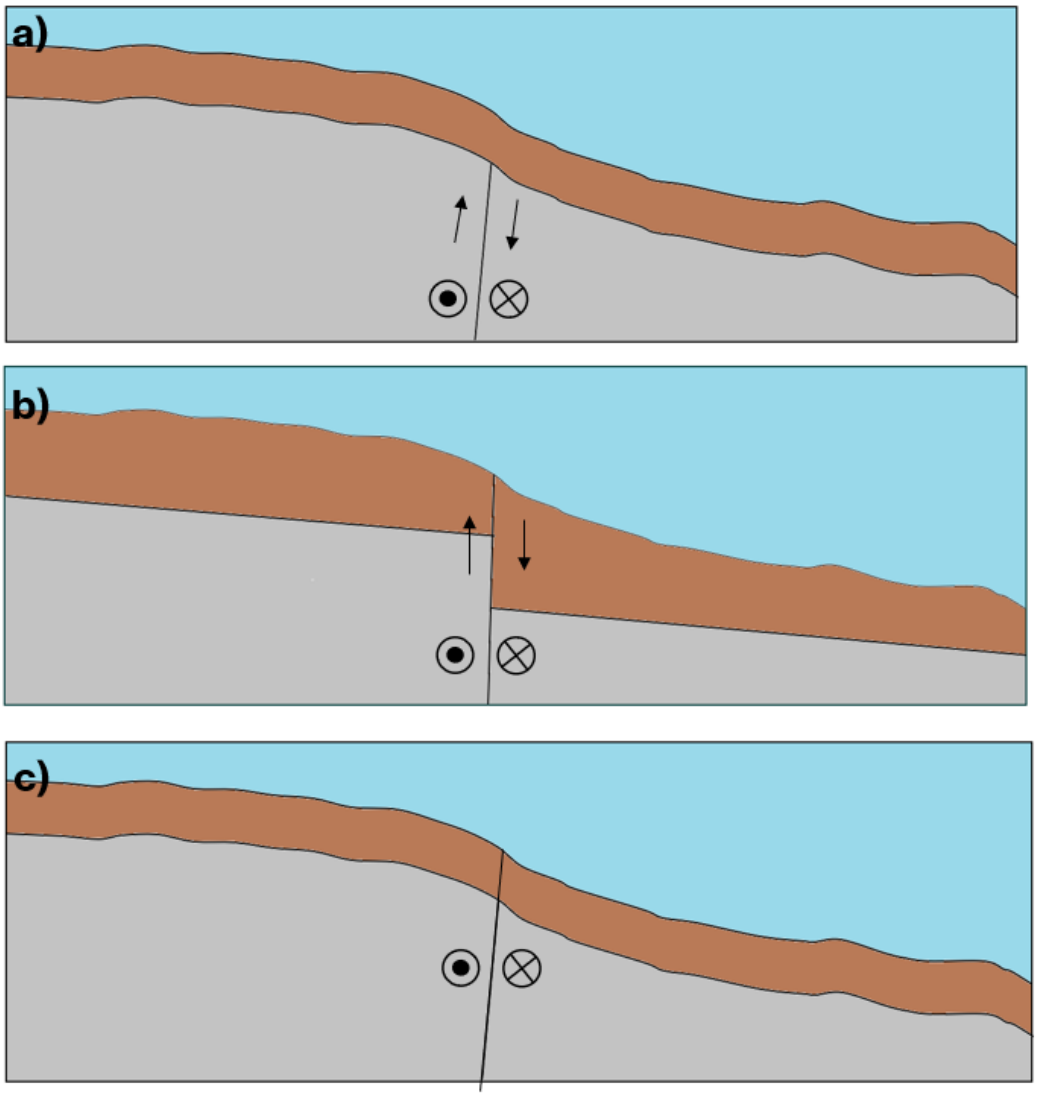

Figure 2.4: Quaternary activity hypothesis.**a)** SJF is inactive, fault buried by undisturbed till. **b)** SJF is active, and slip is vertical or some combination of vertical and horizontal. **c)** SJF is active, and no vertical offset is observed.

3. Methods

3.1 Regional Mapping of Lidar Data

1 m resolution lidar topographic data were compiled for the region along the eastern SJF. Classified point clouds were processed on QGIS software to remove vegetation returns and interpolate ground returns into a DTM, which was then artificially illuminated (QGIS Development Team 2018). This DTM was analyzed between the Koksilah River and Saanich Inlet (Fig. 3.1a) to identify potential fault scarp lineaments, as well as glacial geomorphic landforms such as drumlins and eskers.

As even the largest upper plate earthquakes hosted by faults in this region likely involved slip of only a few meters, the sub-meter resolution of the shaded relief lidar DTM was essential for mapping the surface extent of scarps. Existing fault data from the British Columbia Geological Survey (BCGS) and United States Geological Survey (USGS) were overlain on the DTM for loose reference (Cui et al. 2017, Staisch & Walton 2022). Specifically in the region where the fault bifurcates, disagreement of > 1 km of horizontal distance was observed between the mapped fault and the lineament observed with lidar (Fig. 3.1b). These fault structures were followed and analyzed with particular interest in areas where the apparent fault trace intersected glacial features mentioned above.

Using the lidar data and QGIS software, surface elevation profiles were plotted perpendicularly across suspected fault structures to assess whether each feature may represent vertical displacement of an otherwise planar surface. These profiles were used to identify specific locations where geophysical surveys, such as electric resistivity tomography (ERT), gravity, magnetic, and ground penetrating radar, could be performed.

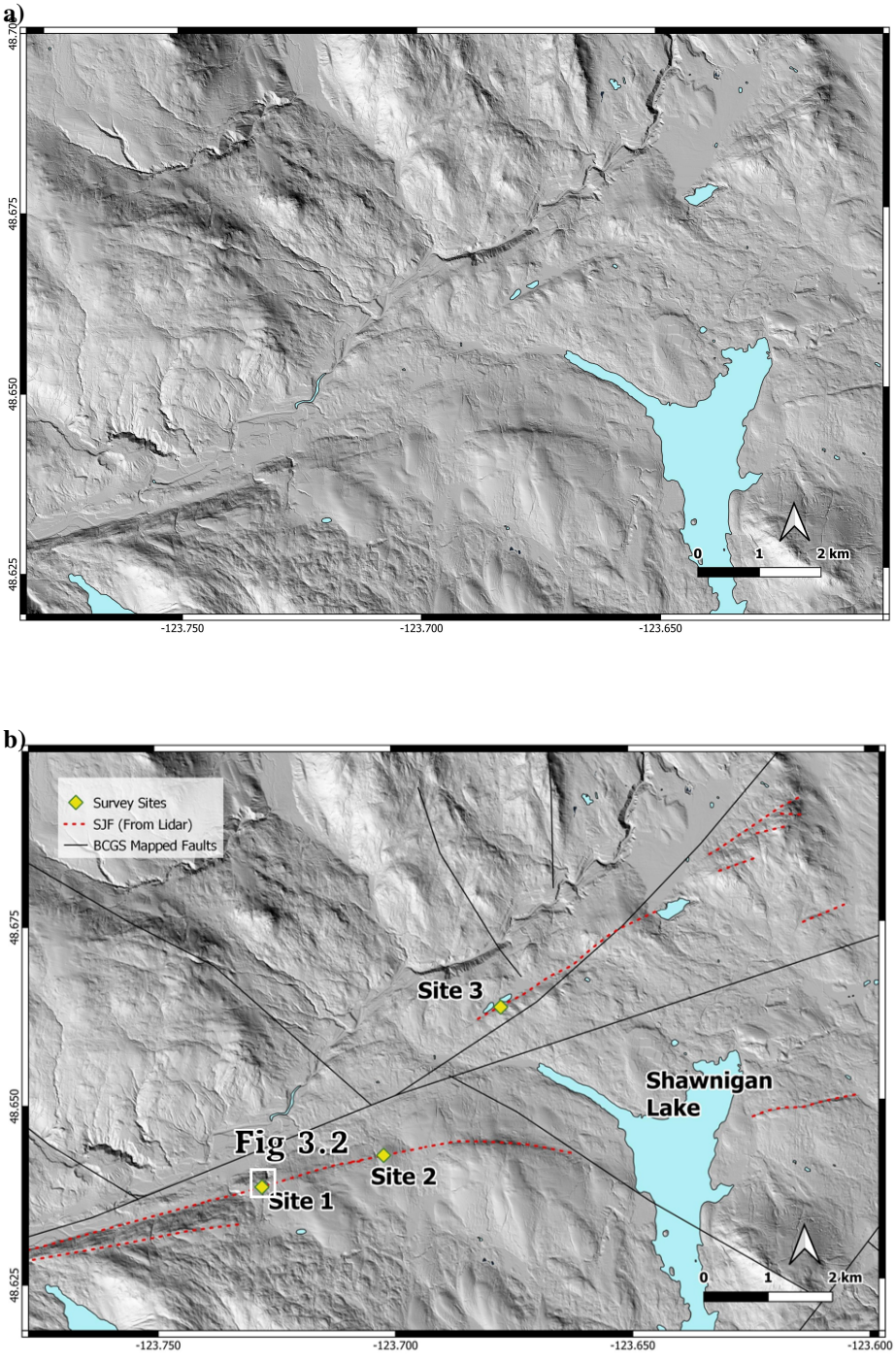

Figure 3.1: **a)** Lidar map of study area. **b)** Same map overlain with survey sites, inferred SJF fault trace, and fault lines from Staisch & Walton (2022) and Cui et al. (2017). Shorelines from Messenger et al. (2016)

3.2 Survey Site Identification

Three sites of interest were located in the region around Shawnigan Lake (Fig. 3.1b). Site 1 appeared to be a fault scarp striking slightly north of east ($080°$). This feature was visible on the shaded relief map as a discontinuous line running approximately 3 km from the Koksilah River to the hills west of Shawnigan Lake. A change in elevation of about six meters can be seen across the main part of the slope, with the topography virtually flattening on either side (Fig. 3.2b). The steepest portion of the slope, with a rise of about 3 meters, is hypothesized to result from a fault rupture, where the terrain south of the fault has been vertically displaced upward with respect to that of the north.

At the location of site 2, approximately 2 km ENE from site 1, a smooth, prominent elliptical, north-trending feature was noticed on the map which truncated the strike of the fault scarp (Fig. 3.1b). This was interpreted as a drumlin. Although the drumlin had the appearance of overlying the fault rather than being offset, this site was selected as a prime location to see if a subsurface discontinuity could be located beneath the drumlin, and if the discontinuity was evident in the both the underlying bedrock and glacial deposits above.

Site 3 was located along the northern branch of the fault trending northeast. The site was situated at the edge of a swamp that lay at the base of a northwest facing slope that was thought to be another possible fault scarp, with the south side of the fault uplifted with respect to the north.

Sites 1 and 3 were accessed on foot for closer inspection in November 2025. We were unable to find suitable vehicle access to anywhere close to site 2. Site 3 appeared to be a swampy basin with sediment fill, and the southern slope was a protruding bedrock feature, possibly a fault scarp but lacking overlying glacial till to test the hypothesis of the study. The slope around site 1 did have the appearance of an offset in an otherwise mostly planar surface of glacial till, which would allow the hypothesis to be tested. We decided to use site 1 as the only survey site to be investigated further.

Elevation profiles were plotted perpendicular to the suspected fault lineaments, approximately 80 m horizontally, centered on the fault. The profile drawn at site 1 can be seen in Fig. 3.2a, where the dotted line marks a clear lineament. The sharp change in elevation corresponded with where the profile intersected the lineament, and this was inferred to represent the location of the fault scarp.

3.3 Geophysical Surveying of Fault Scarp

Geophysical surveys, in particular ERT, have been used to identify shallow subsurface deformation due to faulting that has been later confirmed by trenching, as shown in the discovery of the

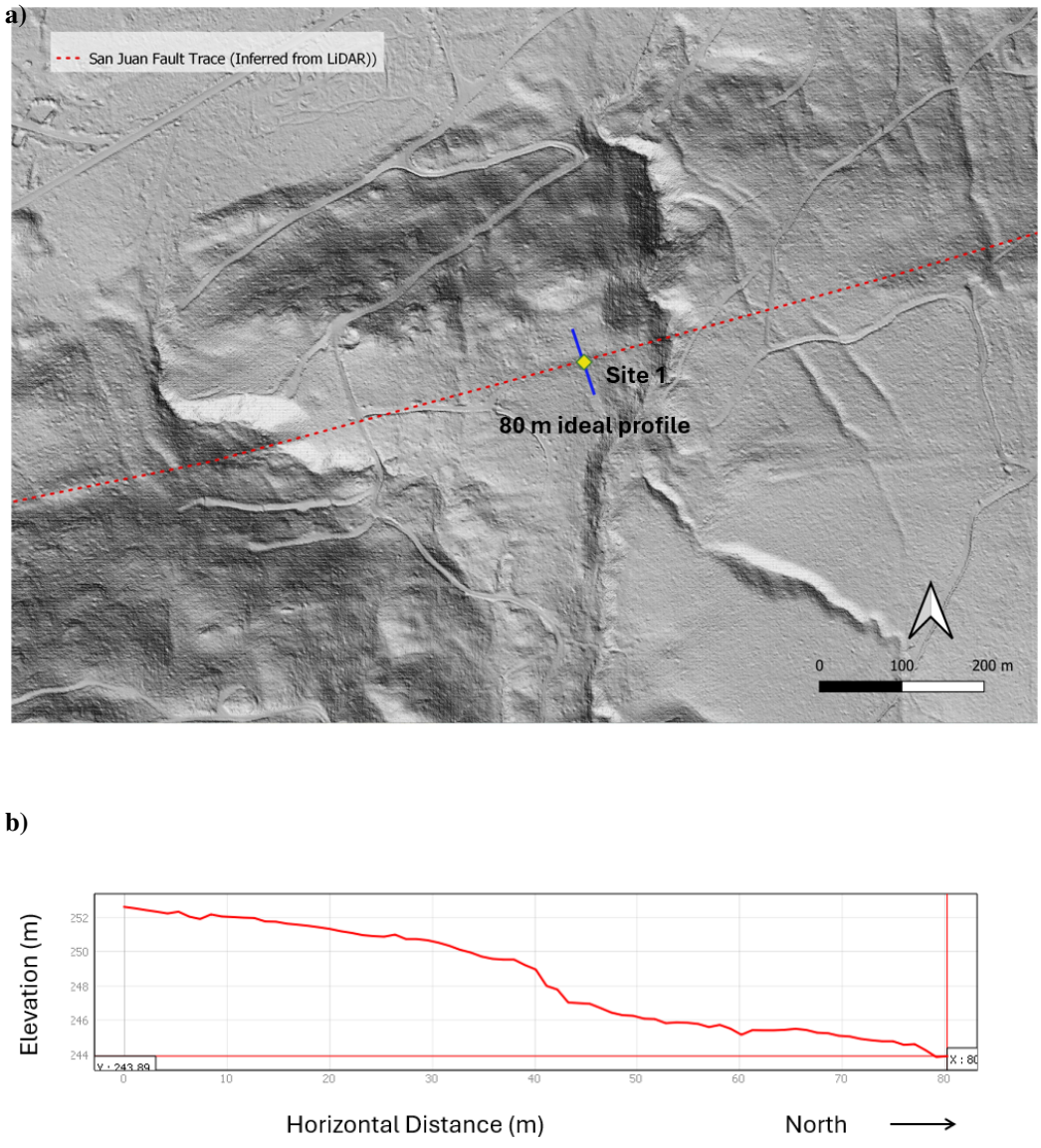

Figure 3.2: **a)** Site 1 survey location with 80 m ideal profile across inferred SJF scarp. **b)** Elevation profile from lidar data of 80 m ideal line; sharp elevation change in the center of the profile was interpreted as a fault scarp.

XEOLXELEK-Elk Lake fault north of Victoria (Harrichhausen et al. 2023). ERT inversions provide 2-dimensional resistivity profiles, which can correspond to subsurface lithologies. The profiles can also show reveal fault structure and how many layers are disrupted. Measuring the total magnetic field across a fault can constrain the sense of the slip. Two vertically offset layers of different magnetic susceptibility can appear as a sinusoidal curve, with the horizontal distance from peak to trough corresponding to the depth to the center of the offset (Kelsey et al. 2012, Burger et al. 2023). Similarly, vertical offset can also produce a density anomaly that can be detected by a gravity survey, producing an arctangent-like curve, with increasing relative gravitation toward the side with higher density nearer to the surface. The steepness of the curve can correspond to the depth to the center of the offset (Burger et al. 2023).

In this study, I used ERT profiles to verify whether the fault structures indeed underlie the suspected scarp, if these structures disrupted the uppermost layer, and if there was vertical offset; I also used total magnetic field and relative gravity data to see if there was corroborating evidence of vertical offset. Geophysical surveys are key in constraining the optimal location for paleoseismic trenching, which is ultimately required to prove whether a fault is active, and to constrain the timing and number of earthquakes associated with a fault scarp. Trenching requires machinery, is expensive and time-consuming, and geophysics data are therefore essential first-order information for determining where to excavate.

3.3.1 Electrical Resistivity Tomography

In January 18, 2026, an 81 meter survey line was mapped out for ERT, selected from the lidar data to be centered on the suspected fault scarp, running perpendicular to the visible linear trend of the feature (Fig. 3.3). This line consisted of 28 electrodes spaced 3 meters apart, in dipole-dipole configuration, able to resolve anomalies with dimensions roughly half the electrode spacing, to a depth of $\sim$ 15 m. An Advanced Geosciences Inc. (AGI) MiniSting resistivity meter and power supply were placed at the northernmost section of the line, which systematically supplied current and measured voltage data, then converted the voltage to apparent resistivity by the following relation (for a four-electrode configuration with current pair *A,B* and voltage pair *C,D*):

$$\rho_a = 2\pi \frac{\Delta V}{I} \left[\left(\frac{1}{r_{AC}} - \frac{1}{r_{BC}} \right) - \left(\frac{1}{r_{AD}} - \frac{1}{r_{BD}} \right) \right]^{-1} \tag{3.1}$$

Where ΔV is the potential difference in volts, *I* is the current in amps, and r_{XY} represents the horizontal distance between electrodes *X* and *Y* in meters (Lowrie & Fichtner 2020). A measuring

tape was laid out in the direction of the survey line azimuth. The south end of the line was selected to be the 0 m mark, and the location of electrode 1, with electrode 28 being placed adjacent to the power supply.

A Focus 6.5" total station was used to measure electrode positions relative to an origin. The total station utilized a laser reflected off a glass prism to provide a relative horizontal and vertical distance from the prism to the station, in meters. The total station was set up a few meters north of electrode 28, and the prism was moved to each electrode to obtain a relative position. Due to lack of line of sight, the total station had to be repositioned to the top of the fault scarp to enable measurement of the southernmost electrode positions.

A 40.5 meter line was also surveyed, along the same line as the longer survey, similarly centered on the suspected fault scarp. This line used a 1.5 meter electrode spacing, to provide a higher-resolution tomographic image of the subsurface beneath the scarp. Electrodes lying within the middle $\sim$ 40 m of the 81 m line were left in place and additional electrodes were placed between them. The new electrode positions were measured with the total station.

To produce true resistivity profiles, the apparent resistivity data were inverted using Earth Imager 2D software by AGI (Advanced Geosciences Inc. 2009). The inversion was performed over 30 iterations until a root-mean-squares misfit between measured and modeled apparent resistivity was minimized.

3.3.2 Relative Gravity Survey

A gravity survey was performed at the same location on January 24, 2026, along roughly the same 80 m line, with several measurements being taken another approximately 60 m north to the volcanic outcrop, as the anomaly of this feature was of interest. A Lacoste-Romberg relative gravimeter was used to obtain relative gravity measurements with respect to a base station chosen as the origin. Using existing markings and the measuring tape, the gravity base station was placed at approximately the same location as the power supply for the ERT survey (Fig. 3.3), and the tape was extended 81 m along the line toward the south (azimuth $155°$). Starting from the base station and working south, gravity measurements were obtained every 5 m until the approximate base of the scarp, at which point the density of readings was increased to every two meters, to provide higher resolution of data overtop the suspected fault structure. The two-meter spacing configuration was begun $\sim$ 30 m south of the base station, and continued to the top of the scarp ($\sim$ 50 m south of base station), at which point the 5 m spacing was resumed.

Gravity measurements were also obtained at four points north of the base station, at 14 m, 27 m, 40 m, and 58 m horizontal distance. The final reading was made on the northern outcrop. The total station was once again used to provide relative vertical and horizontal positions, with the base station treated as the origin. GPS coordinates from the magnetic positional data (section 3.3.3) were used to obtain the base station UTM coordinates. From these, the coordinates for each of the remaining gravity positions were approximated using the measured horizontal distance along strike of the survey line (azimuth $340°$).

The raw data were converted to mGal, and time-dependent corrections for solid-earth tides and instrument drift were applied, after which the base station value (in mGal) was subtracted from these values. (The solid earth tide correction was calculated using a MATLAB script created by Samantha Palmer, University of Victoria, 2016). Corrections were then applied to the data for changing latitude, free-air, and Bouguer plate. Basalt was assumed to be the bedrock for the plate correction, with a density of 2.975 g cm^{-3}. A specific value for rock density of the Duck Lake Sicker group basalt was not available, and the above value was obtained as the average measured density of a dozen other nearby basalt groups in the Canadian Physical Rock Properties database (Enkin 2018). Due to lack of time, terrain corrections were not calculated for these data.

3.3.3 Total Magnetic Field Survey

A magnetic field survey was performed to constrain the location and vertical offset of the suspected rupture. A GEM Systems proton-precession magnetometer was used to measure total magnetic field across the suspected fault traces at several positions. The Earth's magnetic field is sensitive to diurnal variations in the gravitational attraction of the Sun and the Moon (Burger et al. 2023). Base readings were taken from a station fixed at the northern outcrop, to allow these signals to be subtracted away from the local data. These corrections were calculated using GEMLink 5.3 software. The instrument was walked to the southern end of the survey line and back to the base station. Data collection was paused at locations where a walking pace could not be maintained, such as over several large logs. An extensive network of walking trails in the area allowed for several passes of the instrument to be made over the scarp, at varying obliquity. The access trail between the vehicles and the survey site was walked, which crossed the suspected trace. Readings were also taken following a walking trail which proceeded southeast of the northern outcrop, crossing the trace once, then turning northeast and crossing the trace again.

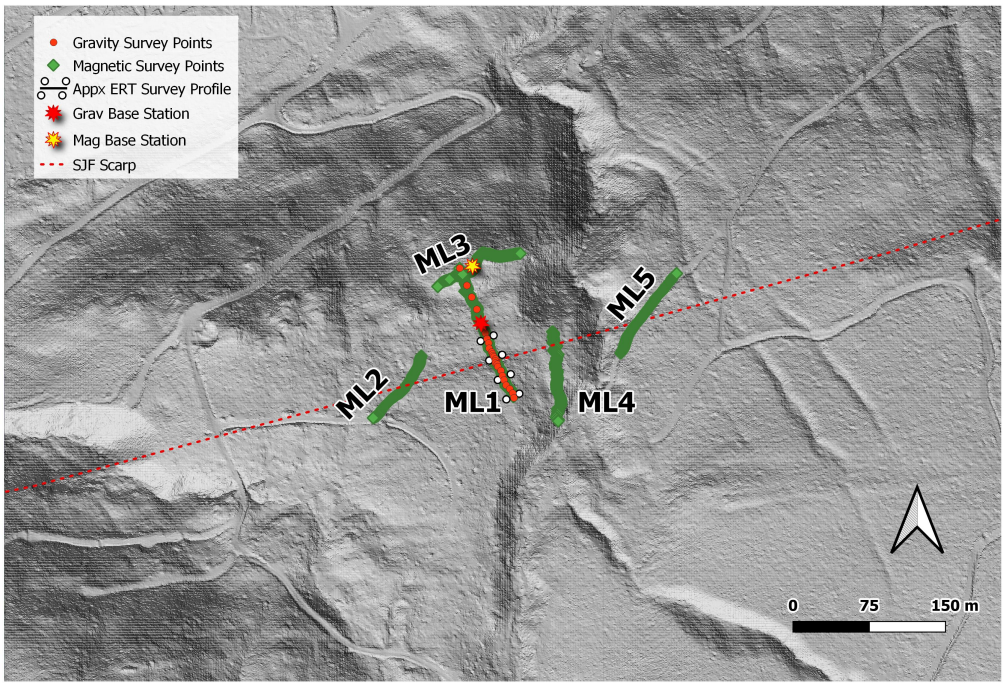

Figure 3.3: Map of geophysical survey lines around site 1. The 5 magnetic lines ('ML') for which plots were produced are shown. A plot of the total field positional data can be found in Appendix A. Note that the ERT profile symbols highlight the extent of the 81 m line for comparison, not two parallel lines.

4. Results

4.1 Electrical Resistivity Tomography Data

A high-resistivity upper layer ($\sim 50,000$ Ω-m) overlies a much lower-resistivity layer (~ 100 Ω-m)(Figs. 4.1a and 4.1b), consistent with glacial till overlying volcanic or intrusive rock (Palacky 1987). Underlying these is a very low-resistivity layer (< 10 Ω-m), interpreted to be the saturated rock below the ground water table. The longer 81 m profile (Fig. 4.1a) shows two parallel features with apparent dip $\sim 75^\circ$ to the south, indicated by low-resistivity anomaly around both structures, but to a greater extent the southern most structure (bottom-left of Fig. 4.1a). These features are interpreted to be fault structures, and the anomalies to be fault gouge, consistent with lower-resistivity clay (Palacky 1987). Various discontinuities in the layering are visible, that also seem to be dipping at a similar angle, showing the possibility of several parallel fault strands.

The steeply-dipping discontinuities are also visible on the 40.5 m profile, and appear in some places to disrupt the uppermost layer as well. Little vertical offset of the layers is visible in either plot. The 40 m profile does not resolve where the fault structures, which were observed on the longer profile, intersect the till layer. These features will be addressed further in the discussion section. A curious wedge-shaped feature is visible around the 26 meter mark, The feature has a lower-resistivity core with a higher-resistivity anomaly two meters deeper, and slightly to the north, and is penetrated by the two strongest disruptions visible in the upper layer.

Both ERT profiles show a curious sawtooth pattern at the boundary of the medium ($\sim$70 Ω-m, light green) and the upper high resistivity unit, more apparent in the 80 m profile. These may result from jointing or foliation in the bedrock.

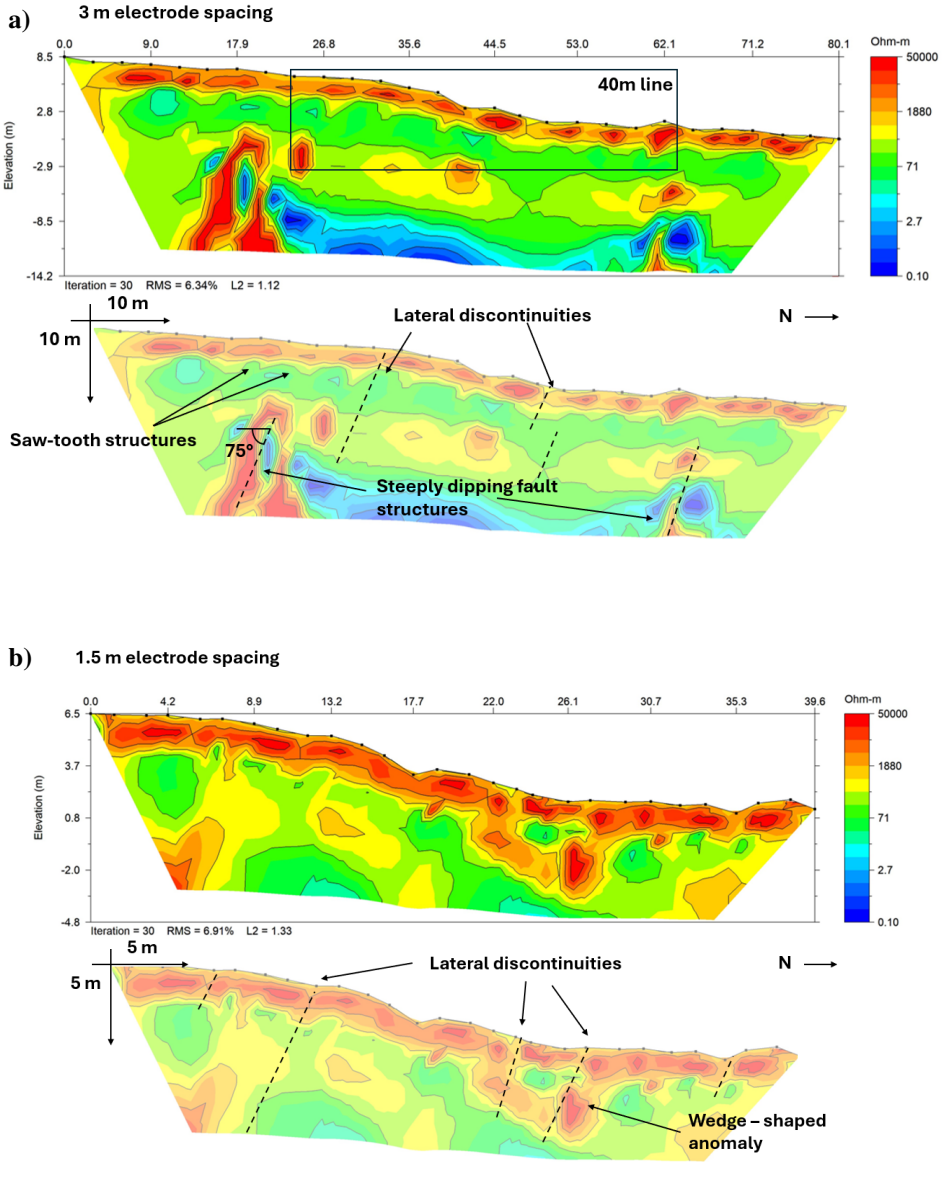

Figure 4.1: a) 81 m electrical resistivity tomography profile, with 3 m spacing of electrodes, with overlay of approximate extent of the 40.5 m profile, and interpretations on lower transparent profile. b) 40.5 m profile with 1.5 m spacing.

4.2 Magnetic and Gravity Data

Analysis of the magnetic field data was done on five different lines (Fig. 3.3), four of which intersected the fault trace, and one (line 3) which ran east to west along the basalt outcrop north of the scarp. Line 1 ran along the strike of the other survey lines from the outcrop to the southernmost ERT electrode. This line was divided into two plots, an 80 m section shown with the longer ERT profile (Fig. 4.2), and a 140 m section plotted alongside the gravity data (Fig. 4.3). For brevity, only these two plots are shown in this section. Plots of the other four lines, as well as the total extent of the magnetic rover data, can be found in Supplemental Figures, in Appendix A.

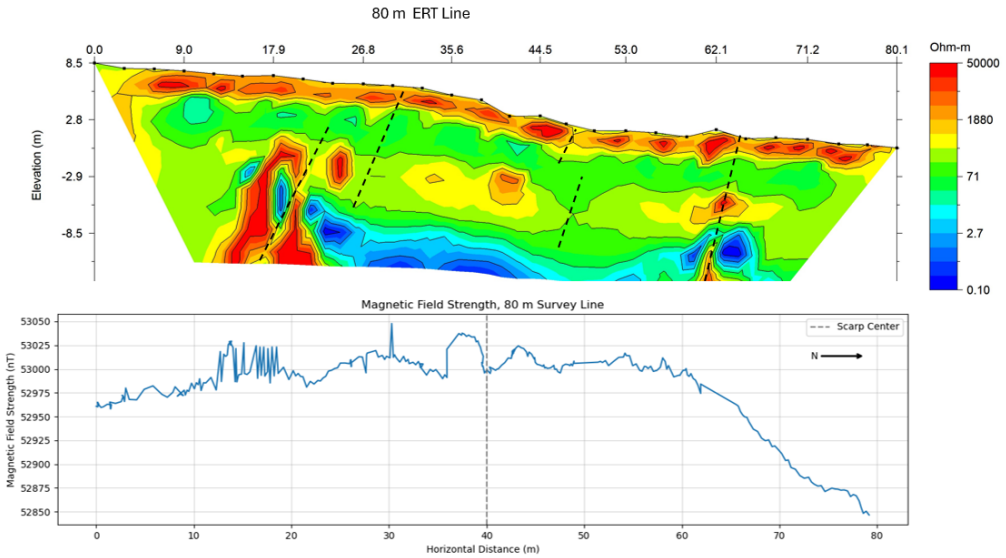

Figure 4.2: 80 meter section of ML1 magnetic data shown below 80 m resistivity line.

The 80 m magnetic line 1 plot (Fig. 4.2) shows a sinusoidal feature with a wavelength of ∼8 m roughly centered on the scarp (x≈40 m). From x=10 m to x=20 m, there is a very short-wavelength anomaly, with peaks ∼30 nT above the adjacent values, that overlies the subsurface fault structure visible on the ERT. Further south, the magnetic field strength gradually decreases by ∼50 nT over 30 m. From x=60 m to x=80 m, there is a sharp decrease of ∼150 nT in the field strength, though the change in elevation is minimal. At various points on this plot and the other magnetic plots, there are sharp deviations corresponding to a single data point, which are noise likely related to jostling of the instrument while collecting the data. The 140 m line (Fig. 4.3) shows a very long wavelength signal that loosely follows the elevation profile, except for a positive anomaly from x=80 m to x=90 m.

Lines 2, 4, and 5 crossed the fault scarp with varying obliquity (Figs. A.2a, A.3a and A.4a), and profiles were made along the path that they were walked as well as a projection onto a line

perpendicular to the scarp. For each line, the northernmost data point was treated as the origin, and lines were roughly straight. A line was drawn on QGIS perpendicular to the scarp that intersected the origin, and the software was used to project the data onto this new line.

Line 2 (Fig. A.2a) shows the strongest lack of correlation with the elevation profile of all the magnetic lines, with a long-wavelength ($\sim$20 m), sinusoidal signal ($\sim$40 nT peak-to-peak, with relative rise in field strength) north of the scarp, and a sharp decrease in field strength north of it. There is an inflection in the field at the scarp, but little correspondence otherwise. This line also shows the lowest variation of amplitude in the field strength (< 100 nT). Lines 4 and 5 (Figs. A.3a and A.4a) both show strong response to the elevation profiles and little notable correlation to the fault intersection, though on line 5, there is a slight positive anomaly at x=63 m. Line 3 (Fig. A.5) has a positive anomaly from x=0 to x=10 m then shows little mostly short-wave fluctuations of which little can be interpreted, though there is a notable lack of correlation with the elevation.

The Bouguer anomaly profile (Fig. 4.3) shows a long-wavelength signal, with a total increase of $\sim$ 2.5 mGal, indicating that subsurface density increases south, possibly interpreted as a change of bedrock across the fault. A small-wavelength signal is visible from x=40 m to x=50 m that may indicate a subsurface shallow-sourced density contrast and/or offset, and is close to where the short-wavelength magnetic anomaly occurs in the magnetic profile. The Bouguer gravity shows a sharp decrease of $\sim$1 mGal near the north end of the profile, where the elevation drops off into a wide valley to the north (Fig. 3.3) and therefore an abrupt absence of mass, which may explain the reduction in gravity. South of the gravity station, the Bouguer curve changes from decreasing to increasing by $\sim$ 0.25 mGal, then begins to decrease again, similarly to the magnetic plot (Fig. 4.3). At the southernmost end there is also an abrupt increase in Bouguer gravity, which is curious, as there was little change in elevation at this location, nor any other abrupt terrain feature. Note that this anomaly only appears at a single station.

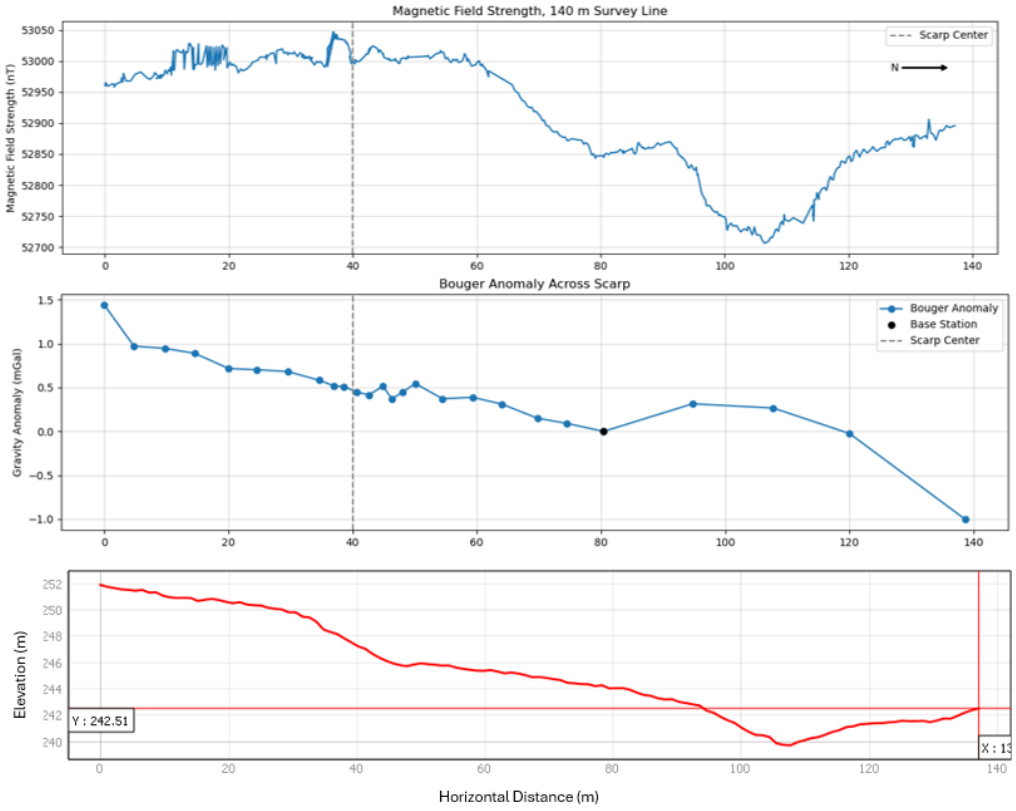

Figure 4.3: 140 m magnetic and Bouguer anomaly data, with elevation profile.

5. Discussion

5.1 Does the San Juan Fault Offset Quaternary Sediments?

The Quaternary activity hypothesis is best examined using the ERT data. In the introduction, three hypotheses were presented. I want to know if the SJF is has been active during the Quaternary, and whether the fault motion was mostly dip-slip or strike-slip. The 81 m profile confirms that a fault zone is present, but the primary strand is curiously not centered underneath the surface scarp. Rather, two parallel steeply-dipping structures were observed, with various discontinuities in the layers visible elsewhere in the profile at similar dip angles. There is no sharp offset visible at the base of the upper (high-resistivity) layer, indicating minimal vertical offset on this contact (See panel 2 of Fig. 2.4). The discontinuities appeared to disrupt the upper high-resistivity layer, interpreted as Quaternary glacial till.

The 40.5 m ERT profile also showed these discontinuities with greater resolution. A large wedge-shaped feature just north of the scarp center was the most interesting feature, adjacent to which were the two most notable discontinuities. The feature has a lower-resistivity core with a high-resistivity anomaly two meters deeper, and slightly to the north. The discontinuities that bound this feature have a dip angle consistent with the deeper fault structures on the 81 m profile, which suggest that these disruptions are likely related.

I interpret the overall profiles to be imaging a fault zone, with little vertical offset to the base of the till but with steeply-dipping disruptions in the till layer. This interpretation argues the fault has ruptured in the Quaternary, and rejects the hypothesis that the scarp was formed by vertical offset, in favour of motion that is mostly strike-slip. Motion of this sense would agree with the suspected kinematics of the SJF mentioned in the introduction. The fact that the two deeper fault structures are not centered beneath the scarp is curious. Possible interpretations of this imaging are 1) a positive flower structure, with dominant lateral motion along the strands clearly imaged by ERT, and minor reverse motion on a strand beneath the fault scarp but invisible to ERT; or 2) entirely strike-slip motion which juxtaposed terrain of different elevation.

To better constrain the geometry of the fault structure in the future, imaging of the intersection of the fault structures with the till layer would be required. This would involve additional short 1.5 m-spaced lines, centered over the intersect points, to be performed. The current 40.5 m profile does

not capture these intersect points. I therefore recommend extending additional 1.5 m survey lines such that shallow high-resolution imaging would be acquired along the full extent of the 80 m profile in Fig. 4.1a.

If additional high resolution profiles show till disruption in more places or even extensions of the fault structures to the surface, and preliminary augering can confirm the lithology of the upper layer adjacent to the discontinuities, then there will be good justification to excavate a paleoseismic trench at this location.

5.2 What Constraints Can Be Provided by the Magnetic and Gravity Data?

The magnetic and gravity data do little to resolve the hypothesis of the report. The most interesting of the magnetic data are the features on the 80 m profile of Line 1 (Fig. 4.2). The short-wave sinusoidal signal lies almost at the center of the fault scarp. A short-wave sinusoidal anomaly curve is characteristic of an abrupt lateral change in magnetic susceptibility, with peak overlying the higher-susceptibility or upthrown unit (Burger et al. 2023). The depth to the center of this feature may be approximated by

$$z = \frac{x(B_{max}) - x(B_{min})}{2}$$

Where $x(B_{max)}$ represents horizontal location of the maximum amplitude of field strength and $x(B_{min})$ the adjacent minimum. For the plot shown in Fig. 4.2, the positive and negative peaks are separated by $\sim$3 m, giving an anomaly depth-to-center of $\sim$1.5 m. This anomaly appears to be centered on the scarp, and consistent with a south-side-up shallow-sourced offset, which is also consistent with the surface scarp. The other feature of interest is the very short-wave anomaly that overlies the deeper fault structure visible near the south end of the 81 m ERT profile, which appears to have a steeply dipping low-resistivity anomaly at its center. The interpretation I make from the magnetic data is therefore supporting evidence that the deeper fault structures are indeed there, with possible slight vertical offset not resolvable in ERT, though due to lack of evidence of vertical offset on any of the other magnetic plots that cross the scarp, I am inclined to favour the interpretation of the ERT profiles, which show no evidence of shallow vertical offset.

The gravity data also display a short-wave low-amplitude anomaly consisting of two adjacent peaks at x$\sim$35 m, which if interpreted as adjacent symmetrical Gaussian peaks would represent two

adjacent shallow spherical anomalies of relatively higher density than their surroundings (Burger et al. 2023). With the resolution of data the depth cannot be stated more accurately than no more than several meters. The horizontal position of this anomaly would place it almost directly above the wedge-anomaly in the ERT. Beyond that, there is little I can confidently interpret without the terrain correction applied, other than a general increase in Bouguer gravity going south, that may represent a lithology change across the fault. It is expected that the bedrock of the West Coast Crystalline Complex, interpreted to be granodiorite (see description of hand samples below), would have density 0.1 to 0.2 g cm^{-3} less than basalt, and be expected to be the lithology south of the fault (Enkin 2018, Cui et al. 2017). Curiously, the Bouguer gravity profile shows the opposite, with a higher relative density inferred toward the south.

A gravel pit was located several hundred meters to the west of site 1 where fault structures were found (Fig. 5.1). Slickenlines (trend/plunge) and fault planes (strike/dip) were observed and measured there. At this location, the SJF is mapped as the contact between the dioritic West Coast Crystalline Complex and basalt, breccia, and felsic tuff of the Duck Lake formation of the Sicker Group (Cui et al. 2017). Rock samples were collected from an outcrop north of the survey line, as well as the gravel pit (Fig. 5.1). The samples from the outcrop were all basalt, likely from the Duck Lake formation. At the gravel pit, basalt was the dominant bedrock, with samples showing heavy weathering and many fracture planes. An outcrop containing granodiorite was also found, likely to be from the West Coast Crystalline Complex. A 1-2 m layer of till was observed above the bedrock at the south end of the gravel pit.

Structural measurements of various features were made at the gravel pit, including fault planes, slickenlines, and foliations. Stereo net plots of these features are presented in Fig. 5.1. Full-page figures of the stereo net plots can be found in Figs. A.7 to A.9. The fracturing and fragmenting of the basalt bedrock samples and the structural measurements suggest the gravel pit intersects a fault zone, though the fault planes show little correlation with the strike of the fault scarp observed on lidar. The slickenlines have steep plunges (60° to 80°) which indicate mostly dip-slip relative block motion. This indicates that this fault zone is perhaps one strand of a larger more complicated structure, or accommodated stress that is much older than the visible scarp.

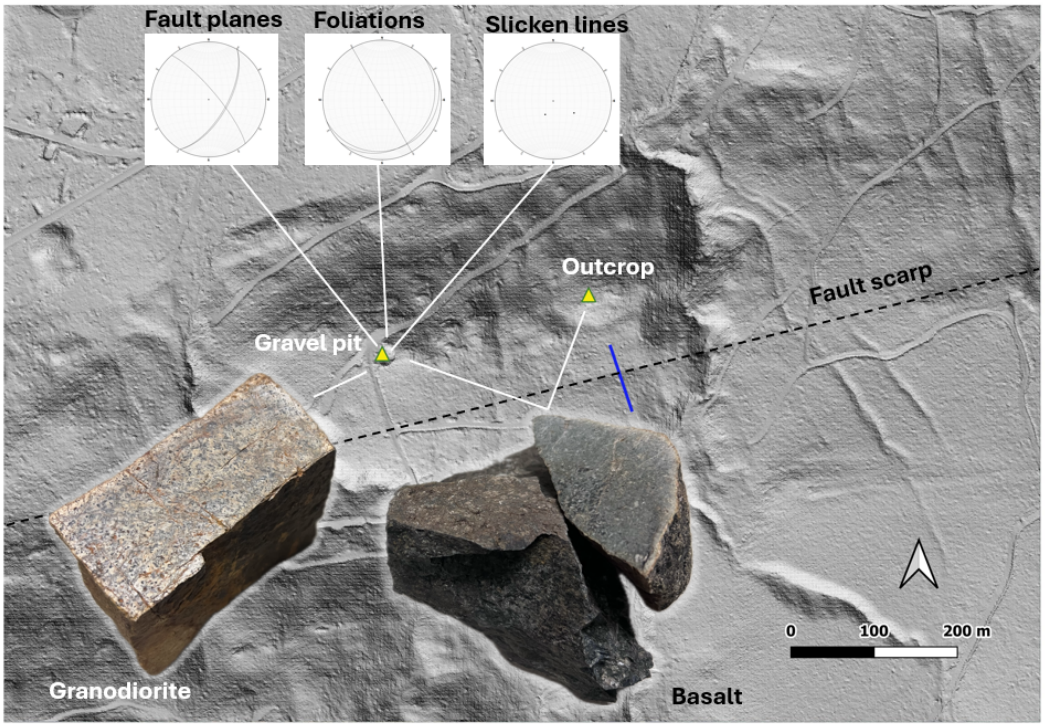

Figure 5.1: Structure measurements made at the gravel pit plotted on stereo nets, and various bedrock samples collected near survey line.

5.3 Seismic Hazard Implications of San Juan Fault Activity

The San Juan fault runs ∼80 km across Vancouver Island, nearby to the most populous region. Using a conservative estimate for rupture width of 15 km, slip of 1.5 m, and shear modulus of granite (22×10^9 N m^{-2}), a full-length rupture of the SJF would produce an earthquake of magnitude $M_w \sim 7.0$ (Wells & Coppersmith 1994, Leonard 2010, Lillie 1999). This would render enormous damage to the nearby communities of Shawnigan Lake, Duncan, and likely Greater Victoria as well. The nearby Leech River fault, which is also terrane-bounding, has been proven to host not only Quaternary, but Holocene earthquakes, as have the Darrington-Devil's Mountain and XEOLXELEK-Elk Lake faults. These upper plate faults appear to accommodate deformation in the forearc, and are in close proximity to the SJF.

The potential size of earthquake the SJF could produce, the likely disruptions in the till layer shown here, and the other corroborating evidence of Quaternary activity by Salomon et al. (2026), demonstrate the need to seek definitive proof that the SJF is active, and constrain its slip rate such that it may be included in seismic hazard models. The great benefit of the site at which my geophysics work was done is its close access for further work. Performing additional 40 m ERT surveys, as well as other geophysical methods, such as ground-penetrating radar or hammer seismic refraction, would be easy to do. If it can be verified with additional data that disruptions exists in the upper layer, and by hand-auger that the resistivity profile relates to the lithology I have interpreted (till overlying bedrock) then the necessary incentive has been provided, and I have identified the ideal location for machine access for paleoseismic trenching.

6. Conclusions and Future work

The size and proximity of the San Juan fault to Greater Victoria and other communities of southern Vancouver Island, as well as other Quaternary-active upper-plate faults, demonstrate the need to constrain its kinematics and the age of earthquakes it has hosted. Evidence of its Quaternary activity was previously documented in the form of stream offset and possible disruption of glacial deposits in the San Juan valley. I identified a fault lineament using lidar data and interpreted steeply-dipping subsurface fault structures in electrical resistivity tomography profiles generated across the feature. The ERT profiles also showed what I interpret to be disruptions in an upper till layer. Minimal vertical offset was observed, consistent with the hypothesis that the lineament is a Quaternary strike-slip dominant rupture. To convincingly prove that the fault is active, paleoseismic trenching is needed. I believe that I have provided a very suitable location to perform this work, as the site is easily accessible by vehicle, but I suggest that further ERT surveys should be carried out for further fault structure imaging, as well as superficial hand-digging near the fault scarp to confirm lithology.

7. Acknowledgements

The author is grateful for the Jamie Cassels Undergraduate Research Award that supported this work. I am also grateful to my supervisors for their support and mentorship throughout. Special thanks are extended to Dr. Guy Salomon for assistance in compiling and processing lidar data and to Yan Anugrah Rahmawan for providing GNSS Velocity data for southern Vancouver Island. Lastly, I am grateful to my colleauges Cameron Louie, Dan Lencki, and Benoit Filion for survey assistance.

Bibliography

Advanced Geosciences Inc. 2009. *AGI EarthImager 2D*. (Version 2.4.0) Retrieved from https://www.agiusa.com/agi-earthimager-2d.

Balfour, N. J., J. F. Cassidy, S. E. Dosso & S. Mazzotti. 2011. Mapping Crustal Stress and Strain in Southwest British Columbia. *Journal of Geophysical Research: Solid Earth* 116(B3). doi: 10.1029/2010JB007828.

Brandon, M. T. 1989. Origin of Igneous Rocks Associated with Melanges of the Pacific Rim Complex, Western Vancouver Island, Canada. *Tectonics* 8(6). 1115–1136.

Burger, H. R, A. F. Sheehan & C. H. Jones. 2023. *Introduction to Applied Geophysics: Exploring the Shallow Subsurface*. Cambridge University Press.

Cassidy, J., G. Rogers, M. Lamontagne, S. Halchuk & J. Adams. 2010. Canada's Earthquakes: 'The Good, the Bad, and the Ugly'. *Geoscience Canada* 37(1). 1–16.

Cui, Y., D. Miller, P. Schiarizza & L. J. Diakow. 2017. British Columbia Digital Geology. Open File 2017-8 British Columbia Ministry of Energy, Mines and Petroleum Resources, British Columbia Geological Survey. Data version 2019-12-19.

DeMets, C., R. G. D. & D. F. Argus. 2010. Geologically Current Plate Motions. *Geophysical Journal International* 181(1). 1–80. doi:10.1111/j.1365-246X.2009.04491.x. https://doi.org/10.1111/j.1365-246X.2009.04491.x.

England, T.D.J. & T. J. Calon. 1991. The Cowichan Fold and Thrust System, Vancouver Island, Southwestern British Columbia. *GSA Bulletin* 103(3). 336–362. doi:10.1130/0016-7606(1991)103<0336:TCFATS>2.3.CO;2. https://doi.org/10.1130/0016-7606(1991)103<0336:TCFATS>2.3.CO;2.

Enkin, R. J. 2018. The Canadian Rock Physical Property Database. Open File 8460 Geological Survey of Canada. doi:10.4095/313389. https://doi.org/10.4095/313389.

GeoBC. 2020. LidarBC Elevation Data. Retrieved from https://lidar.gov.bc.ca/pages/download-discovery. https://lidar.gov.bc.ca/pages/download-discovery.

Goldfinger, C., C. H Nelson, A. E. Morey, J. E. Johnson, J. R. Patton, E. B. Karabanov, J. Gutierrez-Pastor, A. T. Eriksson, E. Gracia, G Dunhill et al. 2012. Turbidite Event History—Methods and

Implications for Holocene Paleoseismicity of the Cascadia Subduction Zone. Tech. rep. US Geological Survey. doi:https://doi.org/10.3133/pp1661F.

Harrichhausen, N., T. Finley, K. D. Morell, C. Regalla, S. E. Bennett, L. J. Leonard & I. Sethnaant. 2023. Discovery of an Active Forearc Fault in an Urban Region: Holocene Rupture on the XEOLXELEK-Elk Lake Fault, Victoria, British Columbia, Canada. *Tectonics* 42(12). e2023TC008170.

Harrichhausen, N., K. D. Morell, C. Regalla, S. E. Bennett, L. J. Leonard, E. M. Lynch & E. Nissen. 2021. Paleoseismic Trenching Reveals Late Quaternary Kinematics of the Leech River Fault: Implications for Forearc Strain Accumulation in Northern Cascadia. *Bulletin of the Seismological Society of America* 111(2). 1110–1138. doi:10.1785/0120200202.

Harrichhausen, N., K. D. Morell, C. Regalla, E. M. Lynch & L. J. Leonard. 2022. Eocene Terrane Accretion in Northern Cascadia Recorded by Brittle Left-Lateral Slip on the San Juan Fault. *Tectonics* 41(10). e2022TC007317. doi:10.1029/2022TC007317. https://agupubs.onlinelibrary.wiley.com/doi/abs/10.1029/2022TC007317. E2022TC007317 2022TC007317.

Kelsey, H. M., B. L. Sherrod, R. J. Blakely & R. A. Haugerud. 2012. Holocene Faulting in the Bellingham Forearc Basin: Upper-plate Deformation at the Northern End of the Cascadia Subduction Zone. *Journal of Geophysical Research: Solid Earth* 117(B3). doi:https://doi.org/10.1029/2011JB008816. https://agupubs.onlinelibrary.wiley.com/doi/abs/10.1029/2011JB008816.

Leonard, M. 2010. Earthquake Fault Scaling: Self-Consistent Relating of Rupture Length, Width, Average Displacement, and Moment Release. *Bulletin of the Seismological Society of America* 100(5A). 1971–1988. doi:10.1785/0120090189. https://doi.org/10.1785/0120090189.

Lillie, R. J. 1999. Whole Earth Geophysics: An Introductory Textbook for Geologists and Geophysicists .

Lowrie, W. & A. Fichtner. 2020. *Fundamentals of Geophysics*. Cambridge university press.

Lynch, E., C. Regalla, K. Morell, N. Harrichhausen & L. Leonard. 2025. Evidence for An Active Transtensional Beaufort Range Fault in the Northern Cascadia Forearc. *Seismica* 2(4). doi:10.26443/seismica.v2i4.1163. https://doi.org/10.26443/seismica.v2i4.1163.

Mazzotti, S., H. Dragert, J. Henton, M. Schmidt, R. Hyndman, T. James, Y. Lu & M. Craymer. 2003. Current Tectonics of Northern Cascadia from a Decade of GPS Measurements. *Journal*

of Geophysical Research: Solid Earth 108(B12). doi:https://doi.org/10.1029/2003JB002653.

McCaffrey, R, A. I. Qamar, R. W. King, R. Wells, G. Khazaradze, C. A. Williams, C. W. Stevens, J. J. Vollick & P. C. Zwick. 2007. Fault locking, Block Rotation and Crustal Deformation in the Pacific Northwest. *Geophysical Journal International* 169(3). 1315–1340. doi:10.1111/j.1365-246X.2007.03371.x.

Morell, K. D., C. Regalla, C. Amos, S. Bennett, L. Leonard, A. Graham, T. Reedy, V. Levson & A. Telka. 2018. Holocene Surface Rupture History of an Active Forearc Fault Redefines Seismic Hazard in Southwestern British Columbia, Canada. *Geophysical Research Letters* 45(21). 11,605–11,611. doi:https://doi.org/10.1029/2018GL078711. `https://agupubs.onlinelibrary.wiley.com/doi/abs/10.1029/2018GL078711`.

Nelson, A. R., B. F. Atwater, P. T. Bobrowsky, L. Bradley, J. J Clague, G. A. Carver, M. E. Darienzo, W. C. Grant, H. W. Krueger, R Sparks et al. 1995. Radiocarbon Evidence for Extensive Plate-Boundary Rupture About 300 Years Ago at the Cascadia Subduction Zone. *Nature* 378(6555). 371–374.

Palacky, G. J. 1987. *Resistivity Characteristics of Geologic Targets. In M. N. Nabighian J. D. Corbett (Eds.), Electromagnetic Methods in Applied Geophysics: Volume 1, Theory*. Society of Exploration Geophysicists. doi:10.1190/1.9781560802631.ch3.

Personius, S. F., R. W. Briggs, A R. Nelson, E. R. Schermer, J. Z. Maharrey, B. L. Sherrod, S. A. Spaulding & L. Bradley. 2014. Holocene Earthquakes and Right-lateral Slip on the Left-lateral Darrington–Devils Mountain Fault Zone, Northern Puget Sound, Washington. *Geosphere* 10(6). 1482–1500.

QGIS Development Team. 2018. Qgis geographic information system. `http://qgis.org`. Open Source Geospatial Foundation Project.

Rahmawan, D. Irwin Y. Zhu L.J. Leonard Y. Jiang J. Elliott, Y.A. 2026. Preliminary Crustal Velocity Field from Expanded Campaign GPS Network on Southern Vancouver Island. *Geological Survey of Canada Open File* (in review, 48p).

Rusmore, M. E. & D. S. Cowan. 1985. Jurassic–Cretaceous Rock Units Along the Southern Edge of the Wrangellia Terrane on Vancouver Island. *Canadian Journal of Earth Sciences* 22(8). 1223–1232. doi:10.1139/e85-124.

Salomon, G., T. Finley, E. Nissen, L. J. Leonard & N. Harrichhausen. 2026. Probable Surface Rupture Along the San Juan Fault in the Recently-deglaciated Northern Cascadia Forearc. Submitted to *Seismica*.

Satake, K., K. Shimazaki, Y. Tsuji & K Ueda. 1996. Time and Size of a Giant Earthquake in Cascadia Inferred from Japanese Tsunami Records of January 1700. *Nature* 379(6562). 246–249.

Staisch, L. M. & M. A. Walton. 2022. Cascadia Subduction Zone Database: Compilation of Published Datasets Relevant to Cascadia Subduction Zone Earthquake Hazards and Tectonics. U.S. Geological Survey Data Release. doi:10.5066/P9O69X6E. https://doi.org/10.5066/P9O69X6E.

Wells, D. L. & K. J. Coppersmith. 1994. New Empirical Relationships Among magnitude, Rupture Length, Rupture Width, Rupture Area, and Surface Displacement. *Bulletin of the Seismological Society of America* 84(4). 974–1002.

A. Supplemental Figures

A.1 Magnetic

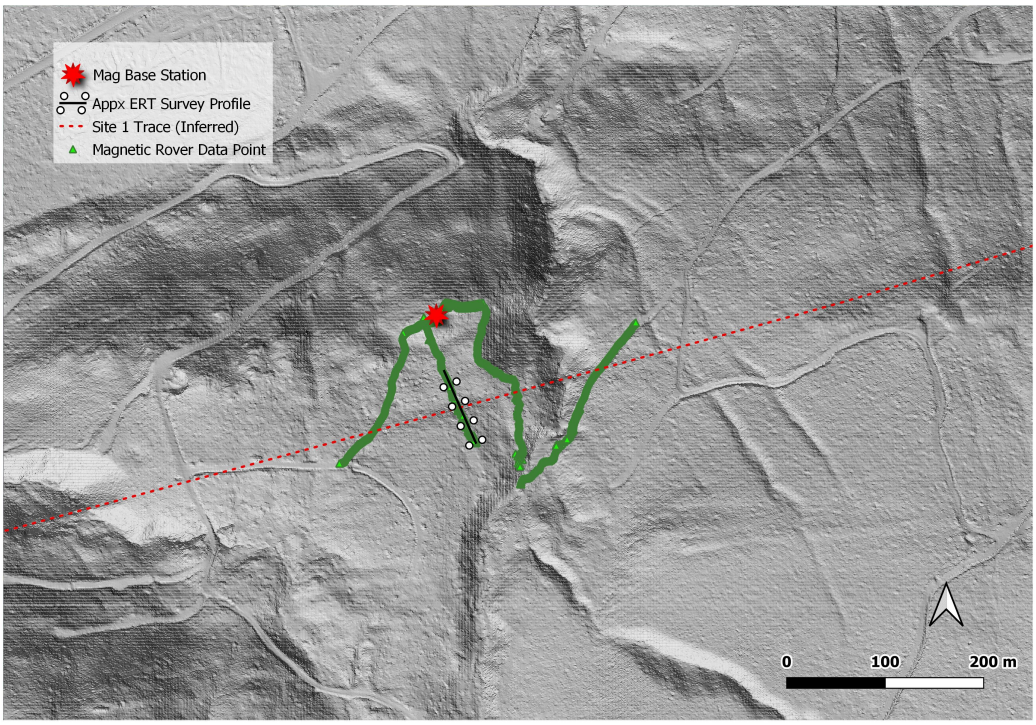

Figure A.1: Map of the entire extent of raw magnetic rover data collected around site one. Lines were truncated be linear at scarp crossings, for better visualization

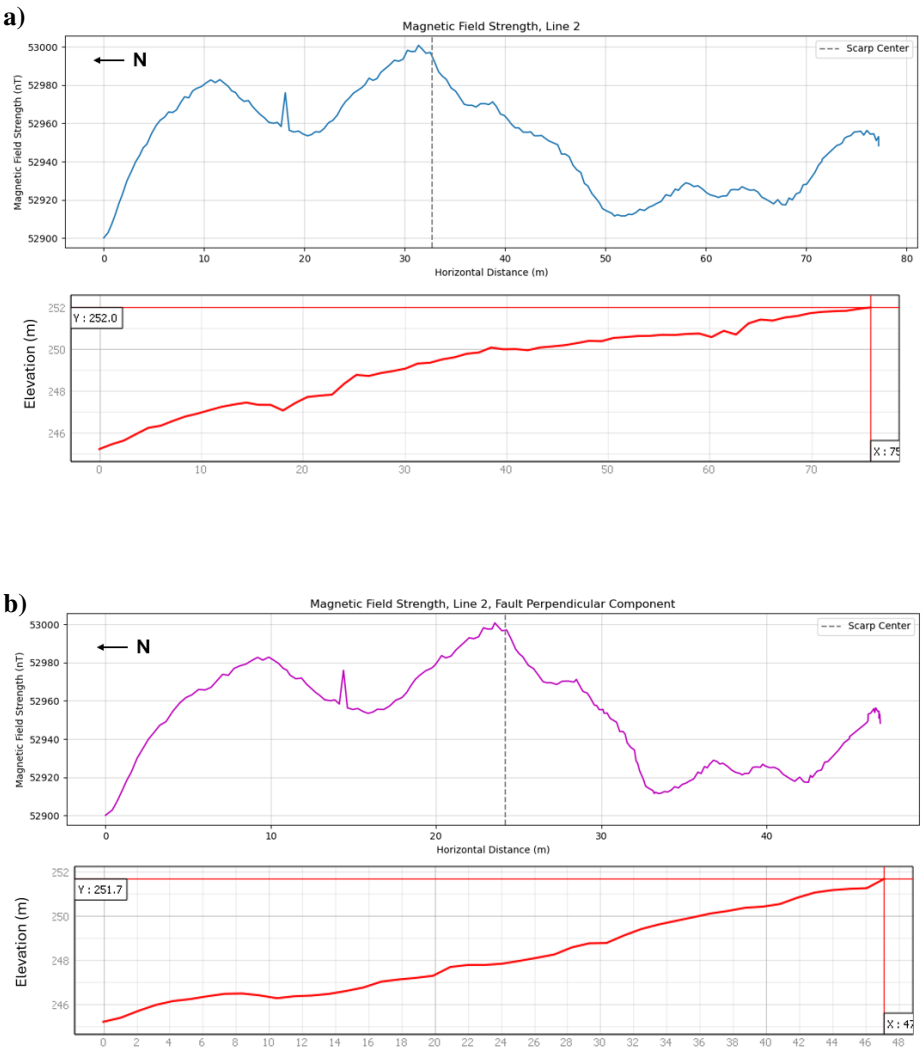

Figure A.2: a) Line 2 magnetic data with elevation along the line shown on Fig. 3.3. b) Line 2 data plotted against a profile projected onto a scarp-perpendicular line.

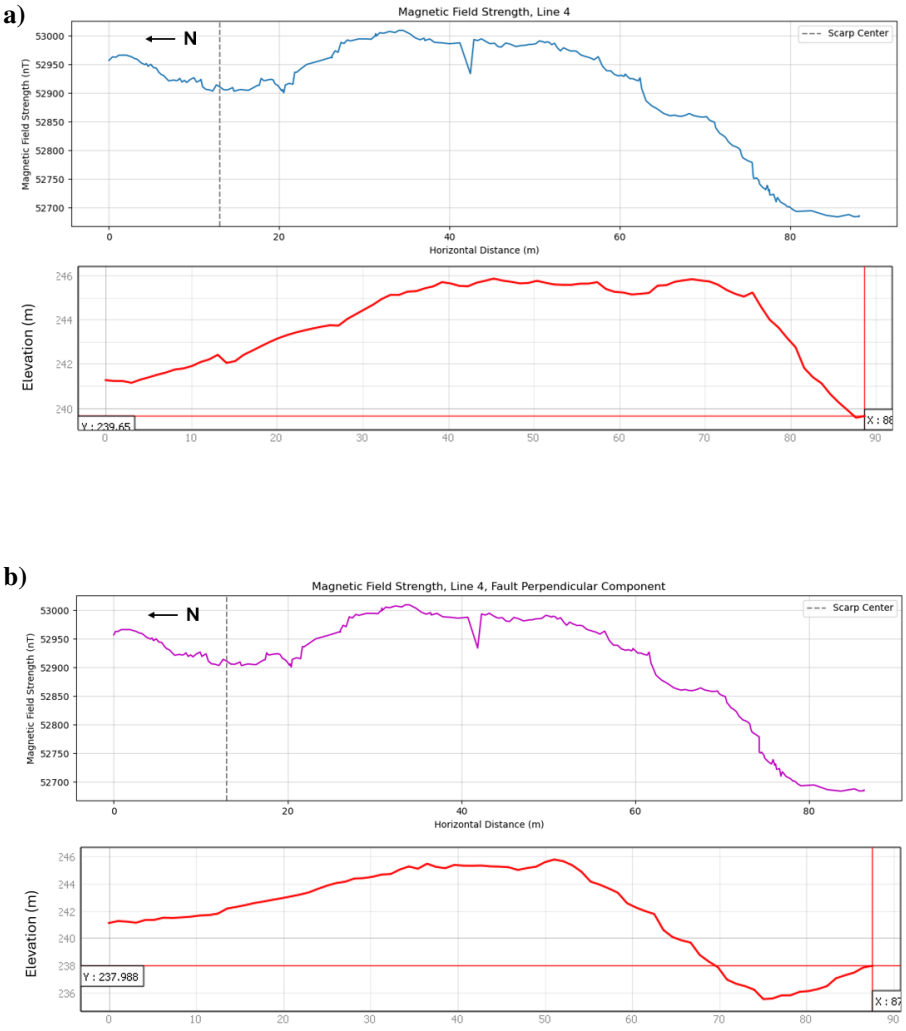

Figure A.3: a) Line 4 magnetic data with elevation along the line shown on Fig. 3.3. b) Line 4 data plotted against a profile projected onto a scarp-perpendicular line.

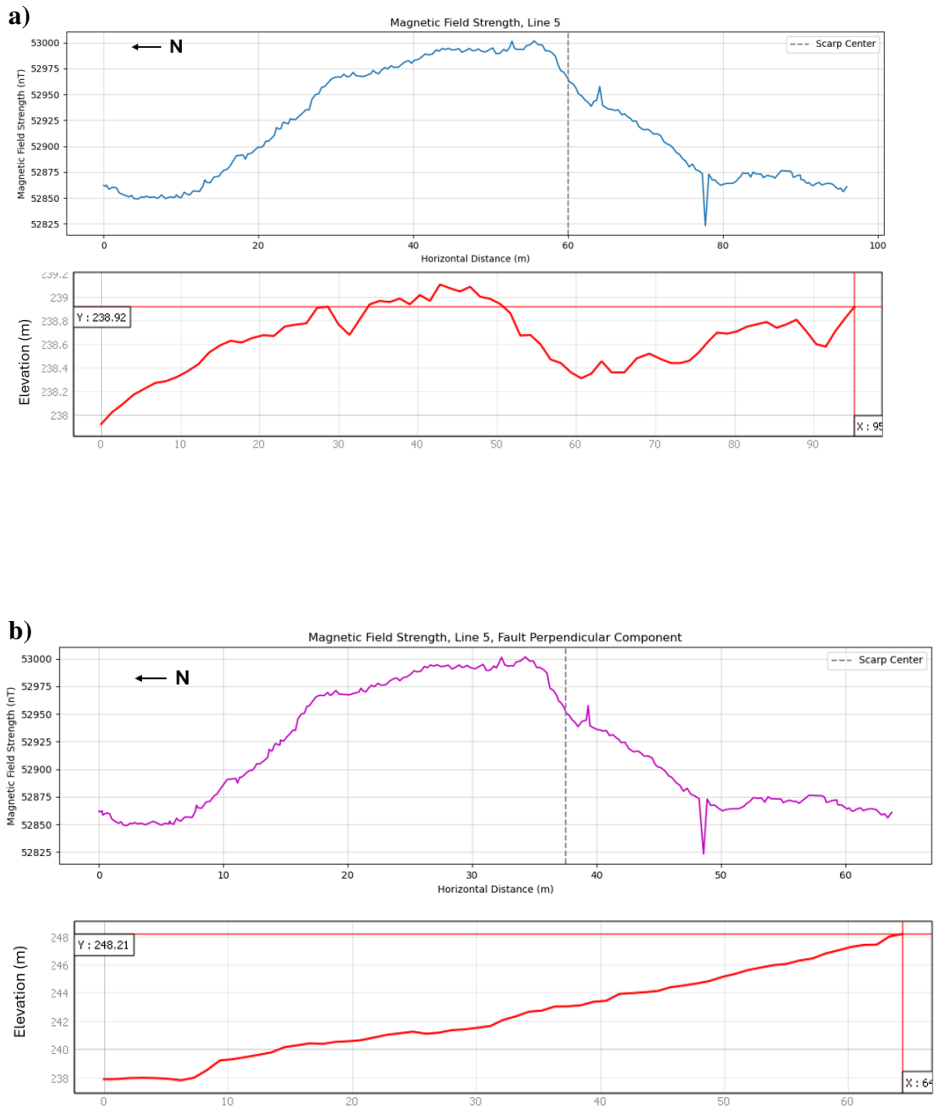

Figure A.4: a) Line 5 magnetic data with elevation along the line shown on Fig. 3.3. b) Line 5 data plotted against a profile projected onto a scarp-perpendicular line.

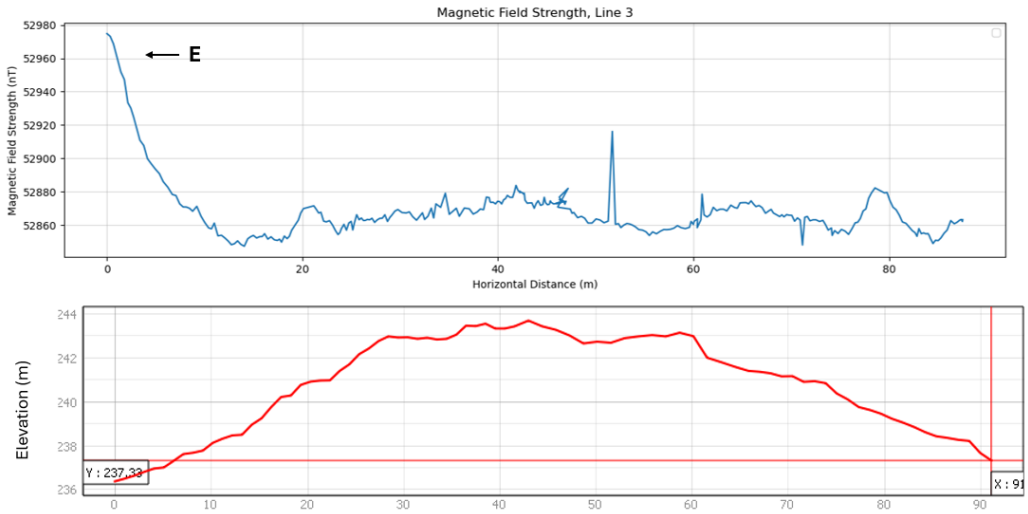

Figure A.5: Magnetic Line three running east-west across the bedrock outcrop north of the fault scarp (Fig. 3.3)

A.2 Gravity

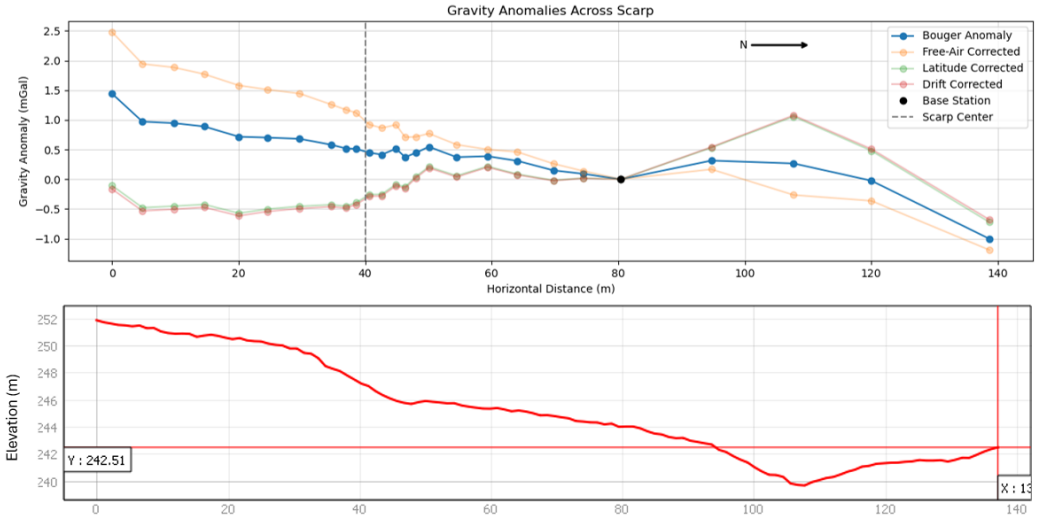

Figure A.6: Gravity anomalies with various corrections that were made shown with elevation profile

A.3 Stereo Net

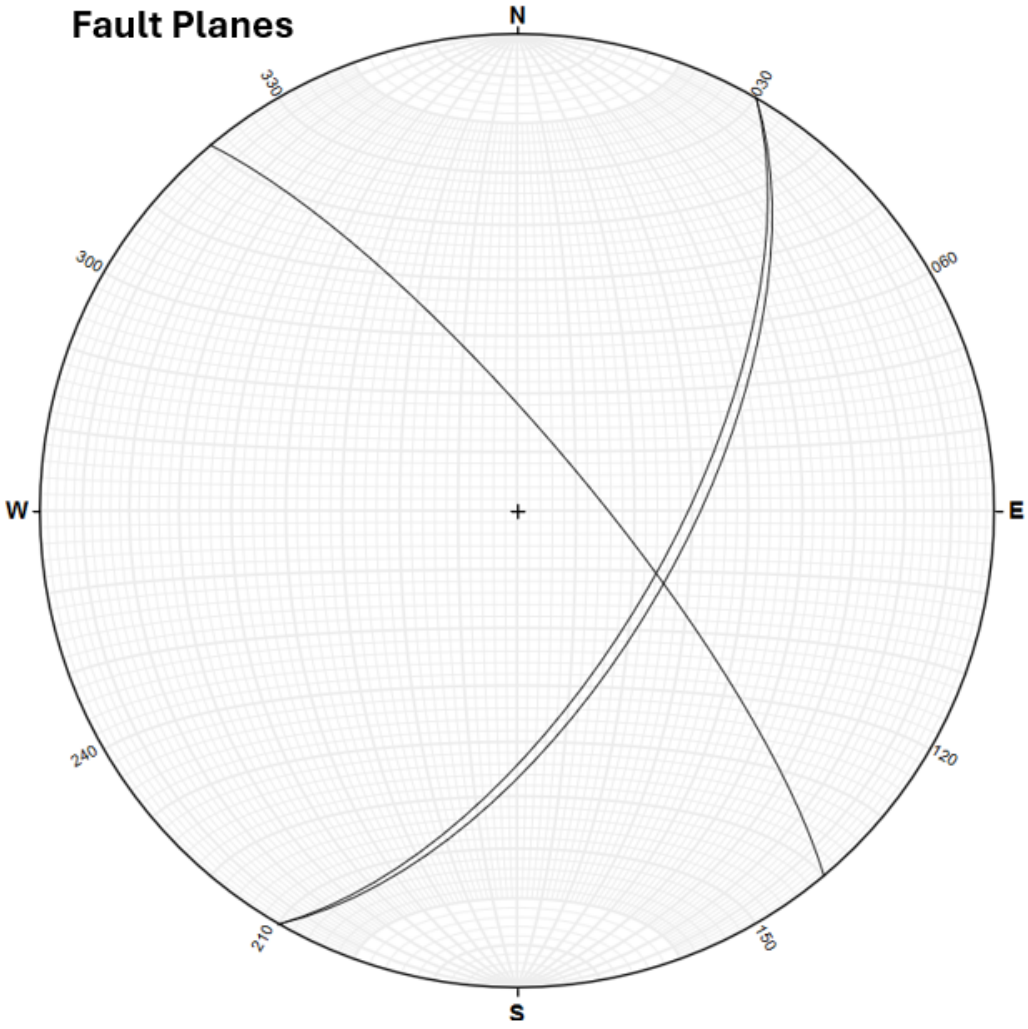

Figure A.7: Geometry of fault planes measured in the gravel pit. Note that lidar scarp strikes $\sim 080°$.

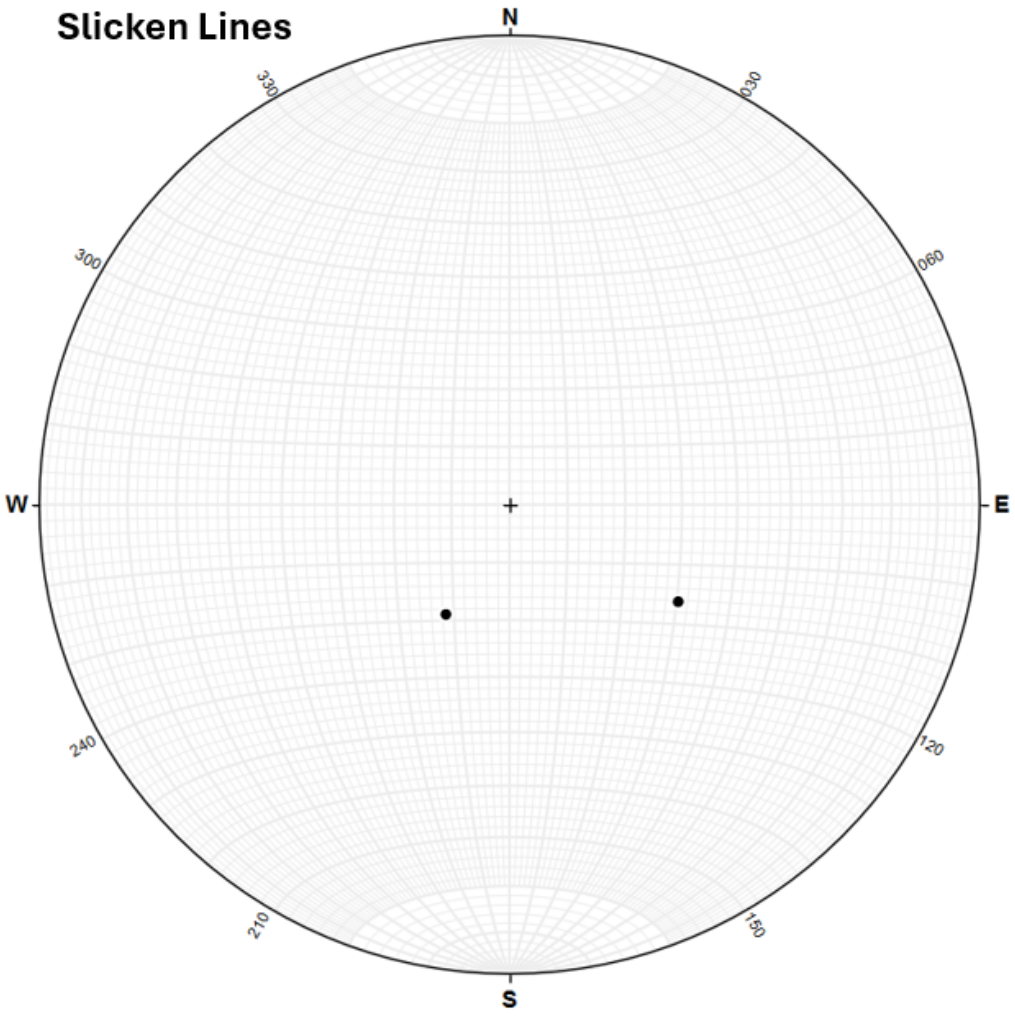

Figure A.8: Slicken lines measured in the gravel pit.

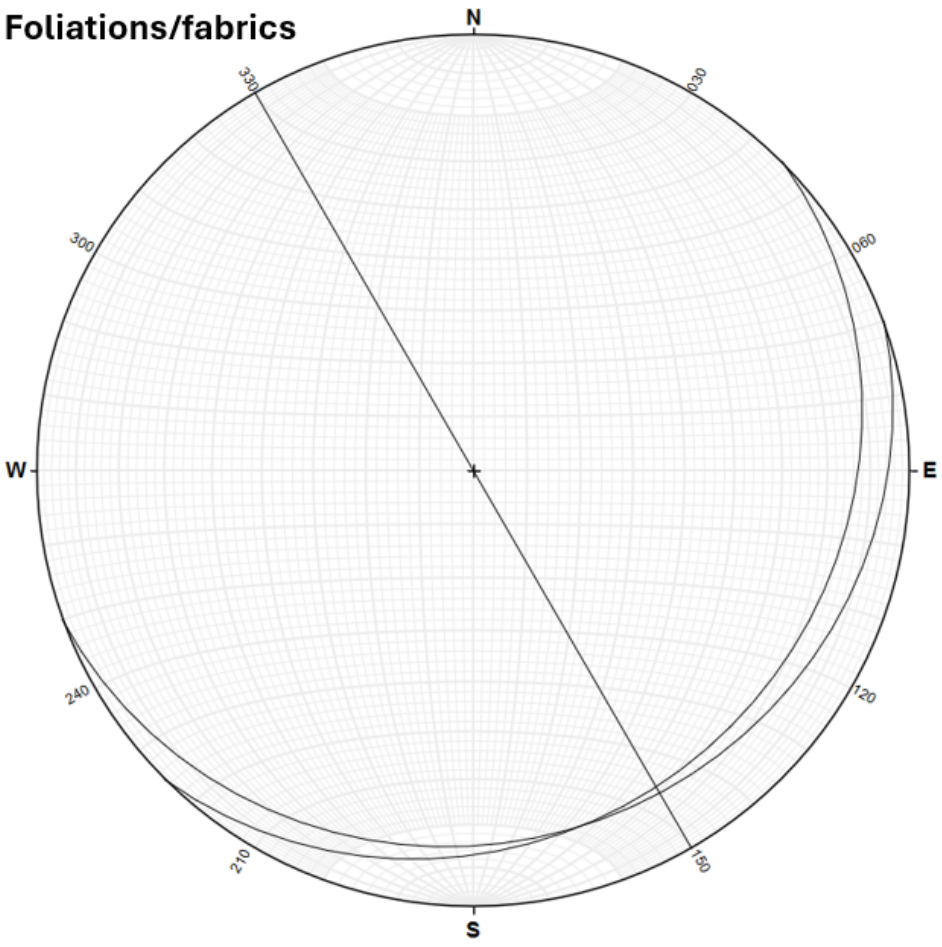

Figure A.9: Foliation planes measured in the gravel pit.